Moving Mesh Kinetic Simulation for Sheared Rodlike Polymers with High Potential Intensities

Yana Di and Pingwen Zhang[*]

LMAM and School of Mathematical Sciences, Peking University, Beijing 100871, P. R. China.

Abstract. The Doi-Hess equation that describes the evolution of an orientational distribution function is capable of predicting several rheological features of nematic polymers. Since the orientational distribution function becomes sharply peaked as potential intensity increases, powerful numerical methods become necessary in the relevant numerical simulations. In this paper, a numerical scheme based on the moving grid techniques will be designed to solve the orientational distribution functions with high potential intensities. Numerical experiments are carried out to demonstrate the effectiveness and robustness of the proposed scheme.

Key words: Orientational distribution function; moving mesh method; spherical geometry; Smoluchowski equation; potential intensity.

1 Introduction

The rheological behavior of rod-like polymers in the nematic phase is analyzed by the Doi-Hess kinetic theory (Doi [5], Hess [9]). A homogeneous population of equal rods is described with an orientational distribution function (ODF). The evolution of the ODF is modeled by the Smoluchowski equation (Doi and Edwards [4]). Once the ODF is known, the rheological response will be determined. It was demonstrated in [10] that under shear flows this theory can give a variety of behaviors for the dynamics of the rod population. The existing numerical schemes include a spectral type method with spherical harmonic functions as basis functions, see, e.g., [7,10,12]. More precisely, the expansion of the ODF in spherical harmonics is truncated at some level l_{max}, and the Smoluchowski equation is reduced to a system of $l_{max}(l_{max}+3)/2$ first-order ordinary differential equations through a Galerkin procedure.

---

[*]Correspondence to: Pingwen Zhang, LMAM and School of Mathematical Sciences, Peking University, Beijing 100871,P. R. China. Email: `pzhang@math.pku.edu.cn`

The intensity of the excluded volume potential U is proportional to the concentration of polymers. When the intensity increases, the ODF becomes sharply peaked and behaves more or less like a δ function. In this case, it is expected that the accuracy of the spherical-harmonic scheme with fixed l_{max} is degraded. Since the accuracy and efficiency of the spectral Galerkin methods rely highly on the solution regularity, higher-order spherical-harmonic functions have to be used in the spectral expansion. However, this may involve a large amount of computational time. In fact, earlier works did not explore high-intensity situations due to computer limitations ([6,7,11]).

The main purpose of this paper is to apply the moving grid technique to resolve the ODF with large potential intensities. In the past few years, it has been demonstrated that the moving mesh methods are very useful in solving problems with singularity, layers, or spikes (see, e.g., [13,14,17]). In this paper, we will also pay particular attention to the rheological features and phase transitions with high potential intensities.

The finite element method on a sphere [15] is used where the basis function is carefully chosen to guarantee the conservation of the ODF. Using the properties of the ODF, we will propose a special moving mesh method for solving the Smoluchowski equation on a sphere. In this respect, it is useful to introduce a vector as the average orientation of the population, the director [4], that serves as a reference for mesh moving. The goal of moving mesh methods is to resolve the small scale of the ODF by clustering more grid points in the smallest scale areas, i.e., around the director. To this end, a two-step scheme is designed: Firstly find the director, rotate the mesh according to the director orientation; this is called 0-d moving; secondly, adjust the mesh according to the numerical solution for ODF; this is called 1-d moving. It is pointed out that the mesh on the sphere is structured in this approach.

The present paper is built up as follows. The Doi-Hess model is introduced in Section 2. The finite element method on the sphere is presented in Section 3. The moving mesh strategy will be described in Section 4. Numerical experiments for high intensities are given in the final section.

2   The Smoluchowski equation

In recent years, the microscopic model has been introduced to study polymeric fluids successfully. Especially, for the rod-like polymer, the Doi-Hess model (Doi [4]) is the most commonly used model, which is capable of predicting several rheological features of rod-like polymers in the nematic phase. In the Doi model, the orientation of a rod is determined by a pseudo-vector $\mathbf{u}$ on the unit sphere, or equivalently by two angles θ and ϕ. A homogeneous population of rod-like, rigid, extremely high-aspect-ratio molecules is described with an orientational distribution function $\Psi(\mathbf{u},t)$. The ODF gives the probability density that a rod is oriented along $\mathbf{u}$ at time t. The evolution of the ODF is modeled with the Smoluchowski equation or the Fokker-Planck equation [4]:

$$\frac{\partial \Psi}{\partial t} = \frac{1}{De}\mathcal{R}\cdot(\mathcal{R}\Psi + \Psi\mathcal{R}V_{ev}) - \mathcal{R}\cdot(\mathbf{u}\times\kappa\cdot\mathbf{u}\Psi), \quad \text{on } \Omega = \mathcal{S}^2 \qquad (2.1)$$

where De is the Deborah number and without loss of generality, is assumed to be 1 as in [6], $\mathcal{R}$ is the rotational gradient operator [1] defined by $\mathcal{R} := \mathbf{u} \times \frac{\partial}{\partial \mathbf{u}}$, κ is the velocity gradient tensor, V_{ev} is an effective excluded-volume potential which is treated with the Maier-Saupe form:

$$V_{ev}(\mathbf{u}) = \frac{3}{2}U \int_\Omega |\mathbf{u} \times \mathbf{u}'|^2 \Psi(\mathbf{u}') d\mathbf{u}'. \tag{2.2}$$

In (2.2), U is the non-dimensional potential intensity. Here, we consider the simple shear flow in Cartesian coordinates (x, y, z) with the velocity in the direction of x, the gradient of the velocity in the direction of z ($\kappa_{13} = G$), and the vorticity in the direction of y. Then κ becomes

$$\kappa = \begin{pmatrix} 0 & 0 & G \\ 0 & 0 & 0 \\ 0 & 0 & 0 \end{pmatrix}, \tag{2.3}$$

where G is the non-dimensional shear rate. Moreover, the orientational distribution function Ψ satisfies

$$\Psi \geqslant 0 \quad \text{and} \quad \int_\Omega \Psi d\mathbf{u} = 1. \tag{2.4}$$

3 The finite element method on sphere

We will project the linear basis functions of the triangles on the polyhedron onto the spherical geodesic triangles. The vertices (anti-clockwise) of a spherical geodesic triangle K are denoted by A, B and C. The plane triangle K_p has the same vertices. For any point P on K, the intersection point of OP and K_p is denoted by W. We define the basis functions on the spherical geodesic triangle K

$$\lambda_1(\mathbf{u}) = \frac{1}{D}(\mathbf{w} \cdot \mathbf{a}_2 \times \mathbf{a}_3), \quad \lambda_2(\mathbf{u}) = \frac{1}{D}(\mathbf{w} \cdot \mathbf{a}_3 \times \mathbf{a}_1), \quad \lambda_3(\mathbf{u}) = \frac{1}{D}(\mathbf{w} \cdot \mathbf{a}_1 \times \mathbf{a}_2), \tag{3.1}$$

where

$$\mathbf{a}_1 = \overrightarrow{OA}, \quad \mathbf{a}_2 = \overrightarrow{OB}, \quad \mathbf{a}_3 = \overrightarrow{OC}, \quad \mathbf{u} = \overrightarrow{OP}, \quad \mathbf{w} = \overrightarrow{OW}, \quad D = (\mathbf{a}_1 \cdot \mathbf{a}_2 \times \mathbf{a}_3),$$
$$\mathbf{w}(\mathbf{u}) = D\mathbf{u}/\mathbf{u} \cdot \mathbf{d}, \quad \mathbf{d} = \mathbf{a}_1 \times \mathbf{a}_2 + \mathbf{a}_2 \times \mathbf{a}_3 + \mathbf{a}_3 \times \mathbf{a}_1.$$

With the given shape functions, we can obtain the finite element space on the sphere,

$$H_h := \left\{ \Psi_h \in C^0(\Omega) : \Psi_h|_K \in \text{span}\left\{\lambda_1, \lambda_2, \lambda_3\right\}, \forall K \right\}. \tag{3.2}$$

Then we have

$$\nabla \lambda_1(\mathbf{u}) = \frac{1}{\mathbf{x} \cdot \mathbf{d}}(\mathbf{a}_2 \times \mathbf{a}_3 - \lambda_1(\mathbf{u})\mathbf{d}),$$
$$\mathcal{R}\lambda_1(\mathbf{u}) = \frac{1}{D}(\mathbf{w} \times \mathbf{a}_2 \times \mathbf{a}_3) - \frac{1}{D}\lambda(\mathbf{u})(\mathbf{w} \times \mathbf{d}). \tag{3.3}$$

Similarly, $\nabla\lambda_2(\mathbf{u})$, $\nabla\lambda_3(\mathbf{u})$ and $\mathcal{R}\lambda_2(\mathbf{u})$, $\mathcal{R}\lambda_3(\mathbf{u})$ can be obtained. It is easy to verify that

$$
\begin{aligned}
\lambda_1(\mathbf{u}) + \lambda_2(\mathbf{u}) + \lambda_3(\mathbf{u}) &\equiv 1, \\
\mathcal{R}\lambda_1(\mathbf{u}) + \mathcal{R}\lambda_2(\mathbf{u}) + \mathcal{R}\lambda_3(\mathbf{u}) &\equiv 0.
\end{aligned}
\tag{3.4}
$$

Denote by $H^1(\Omega)$ the Hilbert space on the sphere with the norm

$$
\|f\|_{H^1(\Omega)}^2 := \|f\|_{L^2(\Omega)}^2 + \|\mathcal{R}f\|_{L^2(\Omega)}^2.
\tag{3.5}
$$

Then H_h defined by (3.2) is a subspace of $H^1(\Omega)$. The weak formation of the equation (2.1) reads as follows: Find $\Psi \in H^1(\Omega)$ such that

$$
\begin{aligned}
&\int_\Omega \frac{\partial\Psi}{\partial t} v d\mathbf{u} + \frac{1}{De}\int_\Omega \mathcal{R}\Psi \cdot \mathcal{R}v d\mathbf{u} \\
&= -\frac{1}{De}\int_\Omega \Psi\mathcal{R}V(\Psi) \cdot \mathcal{R}v d\mathbf{u} + \int_\Omega \Psi(\mathbf{u}\times\kappa\cdot\mathbf{u})\cdot\mathcal{R}v d\mathbf{u}, \quad \forall v \in H^1(\Omega).
\end{aligned}
\tag{3.6}
$$

Following [3], (3.6) can be approximated in H_h semi-implicitly using a three-step Runge-Kutta scheme: Find $\Psi_h^{n+1} \in H_h$ such that

1. Step 1: $\forall v_h \in H_h(\Omega)$,

$$
\begin{aligned}
&\int_\Omega \frac{\Psi_h^{*,1} - \Psi_h^n}{\Delta t/3} v_h d\mathbf{u} + \frac{1}{De}\int_\Omega \mathcal{R}\Psi_h^{*,1} \cdot \mathcal{R}v_h d\mathbf{u} \\
&= -\frac{1}{De}\int_\Omega \Psi_h^n \mathcal{R}V(\Psi_h^n) \cdot \mathcal{R}v_h d\mathbf{u} + \int_\Omega \Psi_h^n(\mathbf{u}\times\kappa\cdot\mathbf{u})\cdot\mathcal{R}v_h d\mathbf{u}.
\end{aligned}
\tag{3.7}
$$

2. Step 2: $\forall v_h \in H_h(\Omega)$,

$$
\begin{aligned}
&\int_\Omega \frac{\Psi_h^{*,2} - \Psi_h^n}{\Delta t/2} v_h d\mathbf{u} + \frac{1}{De}\int_\Omega \mathcal{R}\Psi_h^{*,2} \cdot \mathcal{R}v_h d\mathbf{u} \\
&= -\frac{1}{De}\int_\Omega \Psi_h^{*,1} \mathcal{R}V(\Psi_h^{*,1}) \cdot \mathcal{R}v_h d\mathbf{u} + \int_\Omega \Psi_h^{*,1}(\mathbf{u}\times\kappa\cdot\mathbf{u})\cdot\mathcal{R}v_h d\mathbf{u}.
\end{aligned}
\tag{3.8}
$$

3. Step 3: $\forall v_h \in H_h(\Omega)$,

$$
\begin{aligned}
&\int_\Omega \frac{\Psi_h^{n+1} - \Psi_h^n}{\Delta t} v_h d\mathbf{u} + \frac{1}{De}\int_\Omega \mathcal{R}\Psi_h^{n+1} \cdot \mathcal{R}v_h d\mathbf{u} \\
&= -\frac{1}{De}\int_\Omega \Psi_h^{*,2} \mathcal{R}V(\Psi_h^{*,2}) \cdot \mathcal{R}v_h d\mathbf{u} + \int_\Omega \Psi_h^{*,2}(\mathbf{u}\times\kappa\cdot\mathbf{u})\cdot\mathcal{R}v_h d\mathbf{u}.
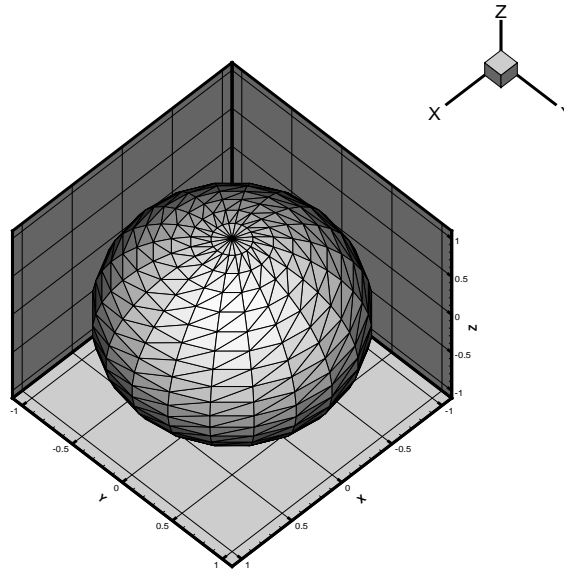\end{aligned}
\tag{3.9}
$$

Figure 1: An illustration of the triangulation.

4 Moving mesh strategy

It is noted that the orientational distribution function $\Psi(\mathbf{u}, t)$ satisfies (2.4). Since $\mathbf{u}$ is a pseudo-vector, we have the following result:

$$\Psi(\mathbf{u}, t) = \Psi(-\mathbf{u}, t), \tag{4.1}$$

which indicates that the ODF is an even function. In the absence of flow, we can obtain from the Smoluchowski equation (2.1) the equilibrium ODF expressed as a Boltzmann distribution:

$$\Psi(\mathbf{u}) = C \exp\left(-V_{ev}(\mathbf{u})\right), \tag{4.2}$$

where C is the normalization constant. At equilibrium, nematics have uniaxial symmetry around a certain direction denoted by a unit vector $\mathbf{n}$ called the "director" that describes the average orientation of the population. There is reflection symmetry with respect to the plane normal to $\mathbf{n}$. As the parameter U increases, the ODF converges to a δ function. In this instance, $\Psi(\mathbf{u}, t)$ has nonzero values only in a small area near the director. These features will be used in designing our special moving mesh finite element method.

4.1 Prepare meshes on a sphere

In this section we will construct a special mesh on spheres. An axis of symmetry is chosen as the polar axis of the spherical mesh and its two opposite ends are set as poles of the mesh. Consequently, the latitudes and longitudes can be defined for the spherical mesh.

Without loss of generality, we may choose the initial director as the polar axis of the spherical mesh. Firstly divide the sphere into $(N+1)E$ grids using N latitudes and E longitudes. Then connect the catercorners of any quadrangle in the mesh to obtain two triangles. This leads to a triangulation consisting of $NE+2$ nodes and $2NE$ elements, see Fig. 1 for a simple illustration. The resulting mesh is non-uniform but structured. In the triangulation, the mesh is dense and has axial symmetry around the director. Such a mesh can be used to approximate the solution effectively.

4.2   Moving mesh scheme

Our special mesh is designed specifically for the problem concerned. In particular, the mesh is determined by the director. Our scheme consists of two steps: Firstly, find the director, and rotate the polar axis of the mesh into that direction. This step is called 0-d moving; secondly, redistribute the latitudes according to the ODF. This step is called 1-d moving. The first step makes the dense area of the special mesh generated by Section 4.1 just around the director and the second step can cluster more grid points in the small scale areas.

4.2.1   0-d moving

Set the polar axis of the mesh as $\mathbf{d}_1$, the new director as $\mathbf{d}_2$, the angle between $\mathbf{d}_1$ and $\mathbf{d}_2$ as ϕ, and the normal vector of the plane constructed by $\mathbf{d}_1$ and $\mathbf{d}_2$ as $\mathbf{n}$. Then we have

$$\mathbf{n} = \frac{\mathbf{d}_1 \times \mathbf{d}_2}{|\mathbf{d}_1 \times \mathbf{d}_2|}, \quad \cos\phi = \mathbf{d}_1 \cdot \mathbf{d}_2, \quad \sin\phi = \sqrt{1 - \cos^2\phi}.$$

We propose to use the following map to rotate the polar axis into the director:

$$\begin{aligned}
\mathbf{r}_{new} &= \mathbf{r}_{old}\cos\phi + \mathbf{n}(\mathbf{n}\cdot\mathbf{r}_{old})(1-\cos\phi) + (\mathbf{n}\times\mathbf{r}_{old})\sin\phi \\
&= \mathbf{r}_{old}(\mathbf{d}_1\cdot\mathbf{d}_2) + \mathbf{n}(\mathbf{n}\cdot\mathbf{r}_{old})(1-\mathbf{d}_1\cdot\mathbf{d}_2) + (\mathbf{n}\times\mathbf{r}_{old})\sqrt{1-(\mathbf{d}_1\cdot\mathbf{d}_2)^2},
\end{aligned}$$

which is called the rotation formula [8]. It rotates the vector $\mathbf{r}_{old}$ by a counterclockwise angle ϕ about an axis $\mathbf{n}$.

4.2.2   1-d moving

Due to the approximate symmetry of the ODF about the director, it is natural to only move the latitudes to the areas near the two poles. The adapted latitude distribution can be viewed as the image of a transformation:

$$\phi = \phi(\xi), \quad \phi = (\phi_0, \ldots, \phi_N)^T, \quad \xi = (\xi_0, \ldots, \xi_N)^T.$$

It is natural to set the integral of the ODF about the longitude as the monitor function:

$$m(\phi) = \int_0^{2\pi} \Psi(\theta, \phi)d\theta. \tag{4.3}$$

Our goal is to construct a quasi-uniform latitude distribution under the new metric, $\{\phi_0^*, \ldots, \phi_N^*\}$. Without loss of generality, we may assume $0 < \phi_i < \pi$ $(0 < i < N)$ and $\phi_0 = \phi_0^* = 0$, $\phi_N = \phi_N^* = \pi$. The equidistribution principle gives

$$\xi(\phi) = \int_0^\phi m(t)dt / \int_0^\pi m(t)dt := F(\phi). \tag{4.4}$$

We will call $F(\phi)$ the latitude distribution function. The new latitude distribution can be obtained by inverting the latitude distribution function. More precisely, $\phi_i^* = F^{-1}(\xi_i)$, with $\xi_i = i/N$, $1 \le i \le N - 1$. Theoretically, finding the inverse can be done by using the Newton method. However, high accuracy for the inverse is not necessary here so we just need use a piecewise linear approximation for F. This yields a fast and easy approach for finding the inverse.

4.2.3 Update the solution on the new mesh

After the mesh redistribution in the physical domain Ω, we need to update the solution Ψ on the new mesh. As proposed by Li et al. [13, 14], we introduce a virtual time variable τ to make the mesh moving process a linear homotopy from the old mesh to the new mesh as τ goes from 0 to 1. Thus the mesh at virtual time τ is $\mathbf{u}(\tau) := \mathbf{u}_{\text{old}} + \tau \delta \mathbf{u}$. In the finite element space, Ψ_h is expressed as $\Psi_h(\mathbf{u}; \tau) = \sum_{i=1}^N \Psi_i(\tau) \lambda_\tau^i(\mathbf{u}, \tau)$, where $\lambda_\tau^i(\mathbf{u}, \tau)$ is the basis function of the finite element space. Direct calculation shows that

$$\frac{d\lambda_\tau^i(\mathbf{u})}{d\tau} = -\delta \mathbf{u} \cdot \nabla_{\mathbf{u}} \lambda_\tau^i(\mathbf{u}), \tag{4.5}$$

where $\delta \mathbf{u} := \sum_{i=1}^N \delta \mathbf{u}_i \lambda^i$. It is expected that the solution updating does not introduce errors of higher orders. To this end, we require that the variant of $\Psi_h(\cdot; \tau)$ to τ will vanish in the test function space:

$$\left\langle \frac{d\Psi_h(\cdot; \tau)}{d\tau}, \Phi_h \right\rangle = 0, \quad \forall \Phi_h \in H_h. \tag{4.6}$$

Using the form of $\Psi_h(\cdot; \tau)$ and (4.5), we get

$$\sum_{i=1}^N \int_\Omega \left\{ \frac{d\Psi_i}{d\tau} \lambda_\tau^i \lambda_\tau^j - \Psi_i \delta \mathbf{u} \cdot \nabla_{\mathbf{u}} \lambda_\tau^i \lambda_\tau^j \right\} d\mathbf{u} = 0, \qquad 1 \le j \le N. \tag{4.7}$$

To match the order of accuracy for the PDE solver, the above ODE system (4.7) can be solved by a three-step Runge-Kutta scheme similar to (3.7)-(3.9).

To summarize, the total moving mesh procedure is as follows:

1. Let $t_0 = 0$. The initial director is given as $\mathbf{m}_0$. Construct a non-uniform mesh on the sphere (Section 4.1) and make 1-d moving (Section 4.2.2) to obtain the initial adaptive mesh using the initial value Ψ_h^0;

2. Use the finite element method on the sphere given in Section 3 to compute the numerical solution $\Psi_h^{(n+1)}$ and the director $\mathbf{m}_{n+1}$ at time step t_{n+1};

3. Use 0-d moving and 1-d moving to obtain the direction and the magnitude of the movement for $\mathbf{u}$. The information is used to move the mesh;

4. Update $\Psi_h^{(n+1)}$ on the new mesh (Section 4.2.3) and go to step 2.

5 Results and discussion

The Doi equation is solved for the time-dependent orientational distribution function of rod-like molecules in a nematic monodomain with high potential intensities. The initial setting is a simple shearing flow with director orientation of various angles with respect to the shearing plane. We find that at low and intermediate shear rates the director can be attracted either to a time-periodic tumbling orbit (or wagging) or to a steady log-rolling state. The final state then depends on the initial director. At high shear rates the ODF achieves a steady state, i.e., flow-aligning.

5.1 Comparison with spherical harmonic expansion methods

The instantaneous average molecular orientation is quantified by the order parameter tensor,

$$\mathbf{S} = \langle \mathbf{uu} \rangle - \frac{1}{3}\mathbf{I}. \tag{5.1}$$

The scalar order parameter $S = (\frac{3}{2}\mathbf{S} : \mathbf{S})^{1/2}$ represents the degree of molecular alignment. S lies in the range $0 \sim 1$, with $S = 0$ for an isotropic phase, and $S = 1$ for rods that are all aligned in the same direction. At thermodynamic equilibrium in the absence of flow, the scalar order parameter S takes on a value, S_{eq}, which depends only on the parameter U. Moreover, $\mathbf{S}$ has uniaxial symmetry; that is,

$$\mathbf{S} = S_{eq}(\mathbf{nn} - \frac{1}{3}\mathbf{I}) \tag{5.2}$$

where the unit vector $\mathbf{n}$ is the director. When considering the dynamics of the orientational distribution function of polymers under external fields, the equation (5.2) is not satisfied. The eigenvector associated with the highest eigenvalue of $\mathbf{S}$ corresponds to the generalization of the director $\mathbf{n}$.

Table 1 shows the values of S_{eq} obtained using both the spherical harmonic expansion method and the moving mesh approach proposed in this work. The value of l_{max} represents the total number of spectral expansion terms. It is not surprising that the accuracy of the spherical harmonic technique with fixed l_{max} is degraded when U is increased. As S_{eq} increases, the ODF Ψ becomes more sharply peaked, and one must use higher-order spherical harmonic functions to represent it. For example, when $U = 100$, the numerical result with $l_{max} = 32$ is not satisfactory. We note that $l_{max} = 32$ implies a set of 560

Table 1: Computed values of S_{eq}.

	$U = 20$		$U = 100$	
Spherical-harmonic expansion	$l_{max} = 20$	0.9444	$l_{max} = 32$	0.8765
	$l_{max} = 24$	0.9460	$l_{max} = 40$	0.9653
	$l_{max} = 28$	0.9461	$l_{max} = 60$	0.9898
	$l_{max} = 32$	0.9461	$l_{max} = 64$	0.9899
Moving mesh method	$N = 20,\ E = 20$	0.9373	$N = 20,\ E = 20$	0.9405
	$N = 30,\ E = 20$	0.9462	$N = 30,\ E = 20$	0.9863
	$N = 40,\ E = 20$	0.9462	$N = 40,\ E = 20$	0.9879
	$N = 50,\ E = 20$	0.9462	$N = 50,\ E = 20$	0.9899

Table 2: CPU time comparison ($U = 10$, $G = 0$, $\Delta t = 0.001$, $T = 1$).

Method	Parameters	CPU time
Spherical-harmonic expansion method	$l_{max} = 28$	$5m20.326s$
Spherical finite element method	Voronoi mesh, 1600 nodes	$22m17.590s$
Moving mesh method	$N = 20,\ E = 20$	$7m20.150s$
Moving mesh method	$N = 15,\ E = 10$	$3m0.420s$

Table 3: CPU time comparison ($U = 100$, $G = 10$, $\Delta t = 0.0001$, $T = 1$).

Method	Parameters	CPU time
Spherical-harmonic expansion method	$l_{max} = 60$	$280m32.058s$
Moving mesh method	$N = 50,\ E = 20$	$133m4.165s$

equations, while $l_{max} = 60$ a set of 1890 equations. In contrast to the spherical-harmonic technique, the accuracy of the moving mesh method does not decrease as fast, since more grids are moved to the area near the director to resolve the small scales of the sharply peaked ODF.

Table 2 gives the CPU time of the spherical-harmonic expansion method, the spherical finite element method on uniform mesh and the special moving mesh method presented earlier for $U = 10$ and $G = 0$. The time step is set as $\Delta t = 0.001$ and total time is $T = 1$. The accuracy of the four schemes in Table 2 is assured to be the same by comparing the values of the scalar order parameter S.

Table 2 shows that the speed-up when using the moving mesh method ($N = 15$, $E = 10$) relative to uniform mesh is about 7, whereas the CPU time for the spherical-harmonic expansion method and the special moving mesh method are almost the same (the ratio between them is about 1.8 : 1). Obviously, the spherical-harmonic expansion method is more effective for low potential intensities. By contrast, for high potential intensities the moving mesh method is the method of choice. And the advantage of the moving mesh method grows with the potential intensity size. Table 3 gives the CPU time of the
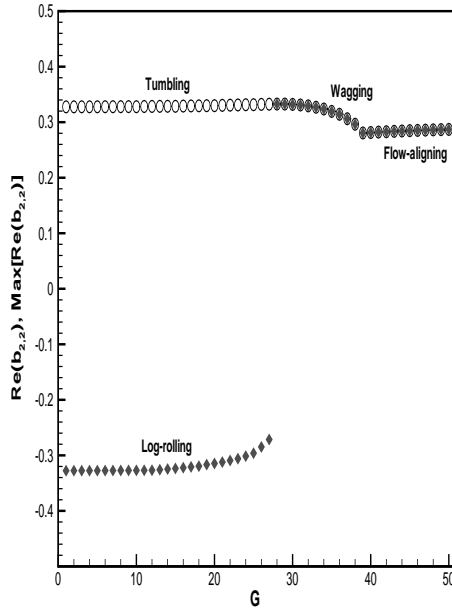
Figure 2: The solution diagram for $U = 10$. In the plots the circle indicates the solutions with an initial director in the shearing plane, the diamond indicates the solutions with an initial director out of the shearing plane. $N = 20$, $E = 20$.
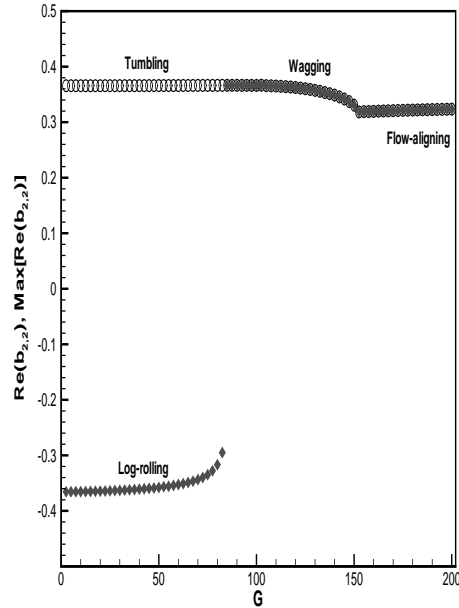
Figure 3: The solution diagram for $U = 20$. In the plot the circle indicates the solutions with an initial director in the shearing plane, and the diamond indicates the solutions with an initial director out of the shearing plane. $N = 30$, $E = 20$.

spherical-harmonic expansion method and the special moving mesh method for $U = 100$ and $G = 10$. The time-step is set as $\Delta t = 0.0001$ and the total time is $T = 1$. In fact, $U = 100$ is almost the limit that the spherical-harmonic expansion method can simulate for PC. So some special treatment has to be considered to avoid the computation beyond the power of PC. But the moving mesh method has not such limitation.

5.2   The flow phase diagram for high potential intensities

The solutions when the shear flow is present are described by plotting two different descriptors of the system state versus the shear rate G. One descriptor is the real part of $b_{2,2}$, the other is the imaginary part of $b_{2,2}$, where $b_{2,2}$ is the coefficient of the spherical harmonic $Y_{2,2}$ of the ODF Ψ. It is easy to verify that

$$\langle \mathbf{uu} \rangle_{11} - \langle \mathbf{uu} \rangle_{22} = 4\sqrt{\frac{2\pi}{15}} Re[b_{2,2}], \qquad \langle \mathbf{uu} \rangle_{12} = -2\sqrt{\frac{2\pi}{15}} Im[b_{2,2}]. \tag{5.3}$$

The former quantity is zero at isotropic state. The imaginary part clearly describes out-of-plane solutions, since it is nonzero when solutions have no symmetry with respect to the shear plane. Of particular interest to us is the quantity $Re[b_{2,2}]$. Because from the
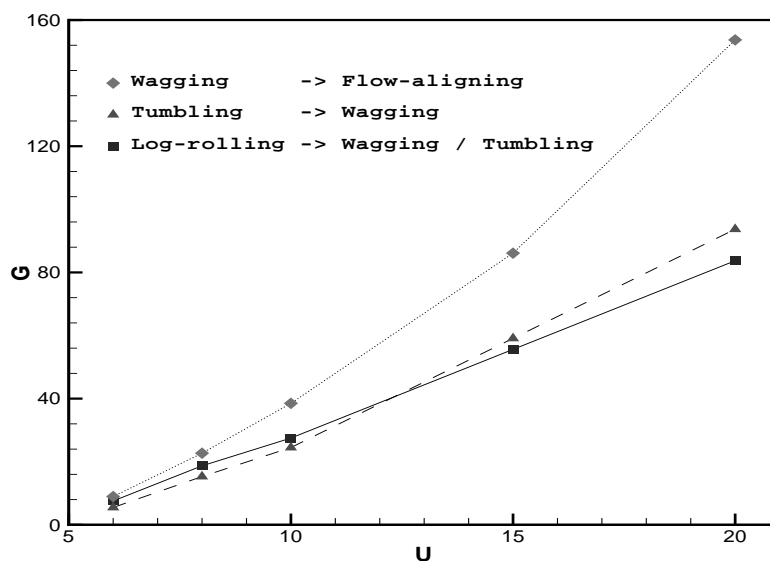
Figure 4: Transition points for different potential rates.

following, for high U, no out-of-plane solutions are found, which shows that $Im[b_{2,2}] = 0$. By plotting $Re[b_{2,2}]$ versus the shear rate G, we can easily distinguish any drift of the molecular orientation either toward or away from the shearing plane or the vorticity axis.

Fig. 2 shows the diagram obtained from the special moving mesh method with $N = 20$ and $E = 20$ for $U = 10$. Fig. 3 shows the situation with $N = 40$ and $E = 20$ for $U = 20$. They are similar in formation. As G is increased, the molecular dynamics goes from tumbling into the wagging regime, i.e., an oscillation of the direction of average molecular orientation between two limiting angles. Above a critical value G_c of G, the shearing plane is the only attractor for the director, while for a range of G below this value both the shearing plane and the vorticity axis are attractors. The critical values of the dimensionless shear rate are $G_c \approx 27.5$ for $U = 10$ and $G_c \approx 83.7$ for $U = 20$. As G is increased further, the director is along the x-axis (the flow velocity direction). This is called "flow-aligning", a steady state direction of average molecular orientation.

The molecular dynamics undergoes some transitions as the shear rate is increased. Fig. 4 shows the transition points for different potential intensities: transition points from log-rolling to wagging (triangles), transition points from tumbling to wagging (squares) and transition points from wagging to flow-aligning (diamonds).

5.3 Some features of $\Psi(\mathbf{u}, t)$ for high potential intensities

Fig. 5 shows the ODF contours for $U = 8$, $U = 10$ and $U = 20$ in the absence of flow ($G = 0$). It is interesting that the ODF has no axial symmetry (as shown in the first line of Fig. 5) even if a symmetrical initial value is given. The equilibrium distributions still
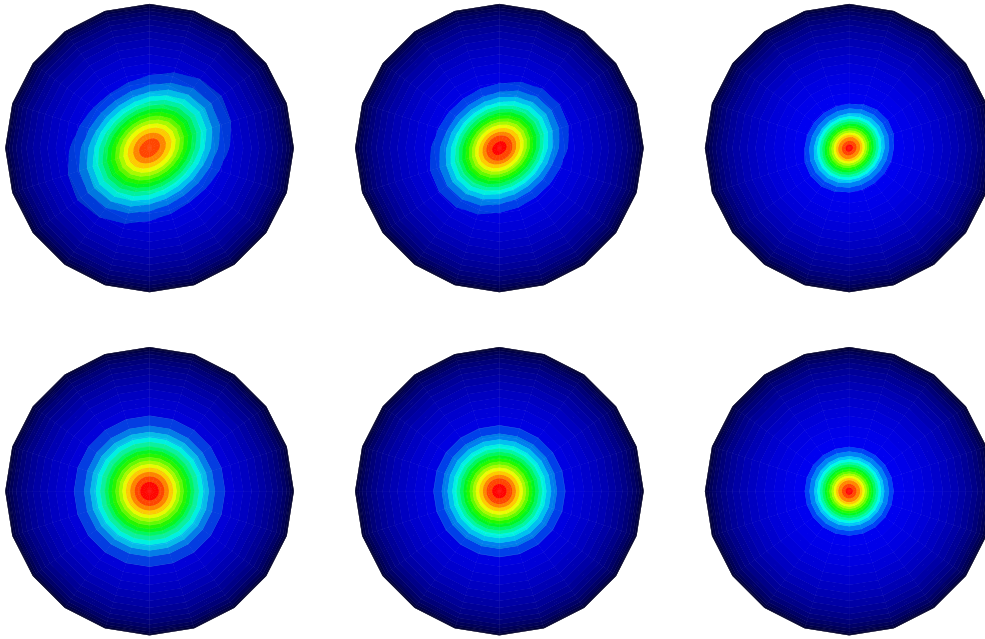
Figure 5: ODF contours for $U = 8$ (left), $U = 10$ (middle) and $U = 20$ (right) in the absence of flow ($G = 0$) at $t = 1.0$ (first line) and $t = 10.0$ (second line).

have the axial symmetry, as shown in the second line of Fig. 5, which is consistent with the theoretical analysis [16]. It can be seen that as the potential intensity is increased, the ODF becomes more peaked.

Fig. 6 shows the evolution of the ODF for $U = 20$ and $G = 50$ in a period. It can be clearly observed that the director tumbles in the shear plane and the ODF changes periodically. In a period, the director rotates slowly when it is adjacent to the flow-direction (x-axis), whereas it rotates fast when it is adjacent to the flow-gradient direction (z-axis). As can be seen, the ODF is most sharply peaked when the director is along the flow-gradient direction (z-axis) and becomes planar gradually when the director rotates from the positive direction of z-axis to the negative one. These can also be found in Fig. 7, because the scalar order parameter S represents the degree of molecular alignment.

Fig. 7 shows S and $Re(b_{2,2})$ versus time for $U = 20$ and different shear rates $G = 25, 50, 75, 100$ with the initial director adjacent to the shearing plane. The shearing plane is defined to be parallel to both the velocity and its gradient. In all cases of Fig. 7, there is a periodic oscillation of S and $Re(b_{2,2})$ which reflects the tumbling or wagging motion of the director. For initial director adjacent to the vorticity axis (y axis), the director drifts toward the vorticity direction; when it reaches it, the log-rolling state is attained; thus S and $Re(b_{2,2})$ do not oscillate but remain nearly constant at a value. So we will not display the corresponding figures.
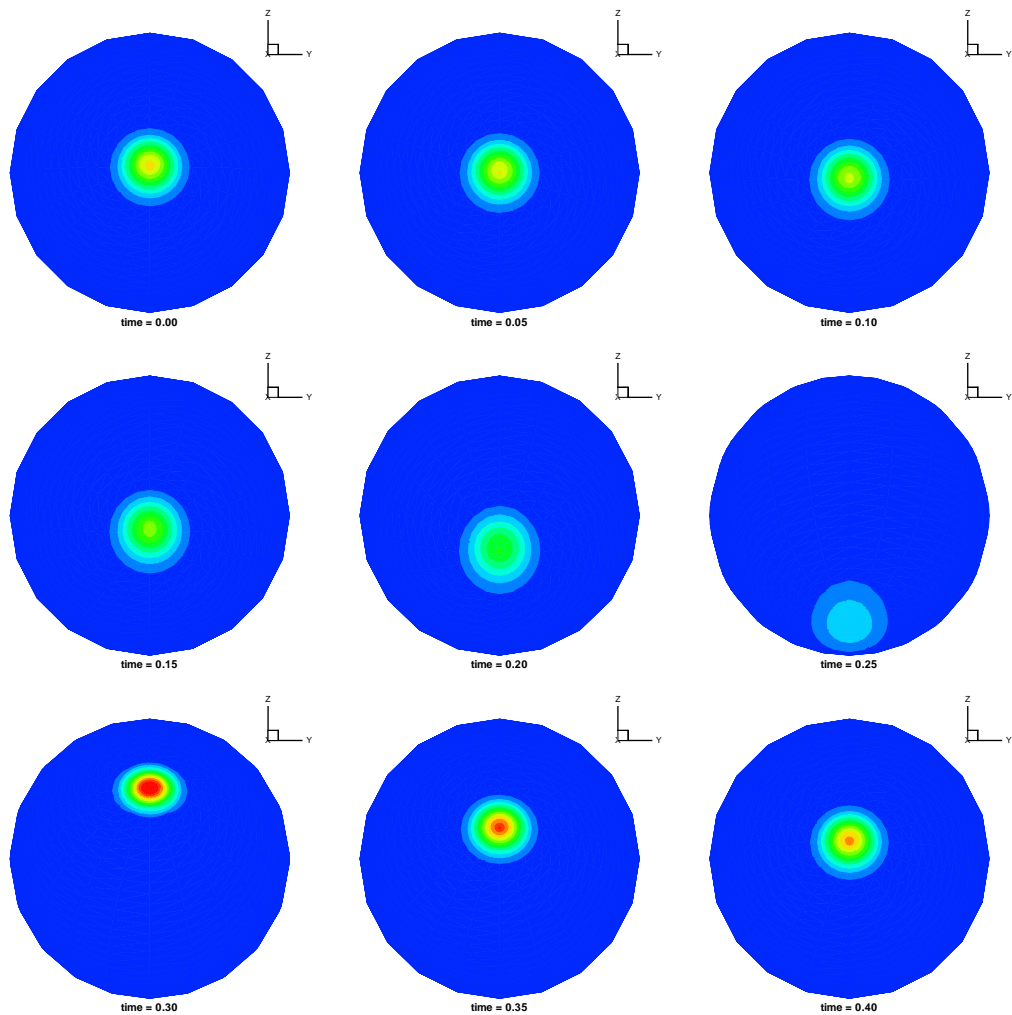
Figure 6: Time sequence of the ODF for $U = 20$ and $G = 50$ in a period. It can be seen that the director tumbles in the shear plane and the ODF changes periodically. Contours are from 0 to 8 by 0.5 and figures are 0.5 apart.

6   Conclusions

In this paper, we have developed a moving mesh strategy useful for nematic polymer kinetic simulations with high potential intensities under shear flows. This strategy fully utilizes the properties of the orientational distribution function, which makes the moving mesh method more effective than a general moving mesh method. We also investigated some rheological features of nematic polymers for high potential intensities using the proposed moving mesh method.

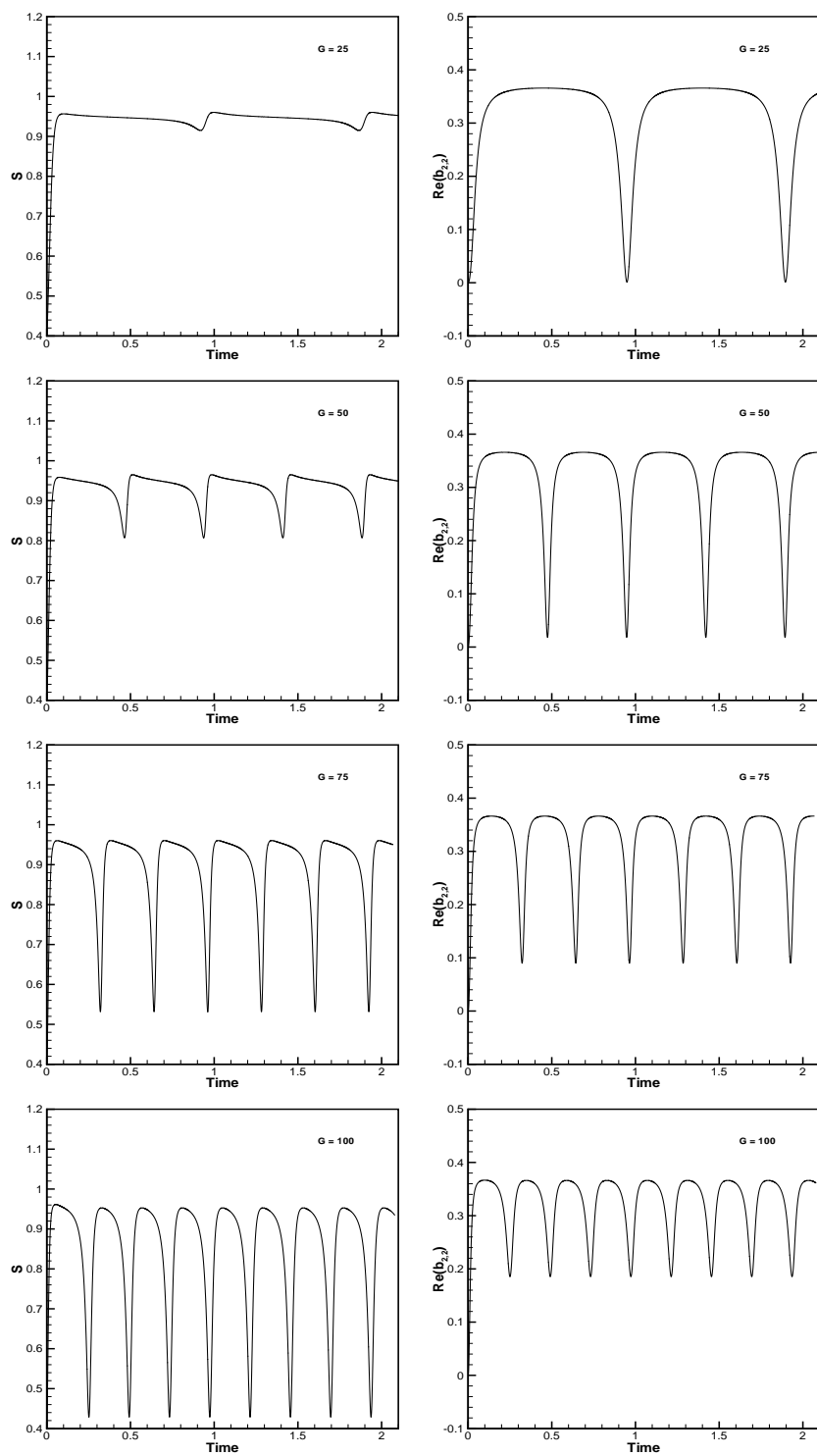It is now well known [10] that, under shear flows, the dynamics of the rod population

Figure 7: S (left) and $Re(b_{2,2})$ (right) vs time for $U = 20$ and different shear rates.

presents a variety of behaviors. However, due to the computer limitation the understandings for high potential intensities are still lacking and further research along this direction is still required. It is believed that our moving mesh method is useful in performing robust and accurate simulations for this problem.

Acknowledgments

References

[1] B. Bird, R. C. Armstrong and O. Hassager, Dynamics of Polymeric Liquids, Vol. 1, Fluid Dynamics, 2nd ed., Wiley, New York, 1987.
[2] E. U. Condon and G. H. Shortley, The Theory of Atomic Spectra, Cambridge University Press, 1979.
[3] Y. Di, R. Li, T. Tang and P.-W. Zhang, Moving mesh finite element methods for the incompressible Navier-Stokes equations, SIAM J. Sci. Comput., 26 (2005), 1036-1056.
[4] M. Doi and S. F. Edwards, The Theory of Polymer Dynamics, Oxford University Press, 1986.
[5] M. Doi, Molecular dynamics and rheological properties of concentrated solutions of rodlike polymers in isotropic and liquid crystalline phases, J. Polym. Sci. Polym. Phys. Ed., 19 (1981), 229-243.
[6] V. Faraoni, M. Grosso and S. Crescitelli, The rigid-rod model for nematic polymers: An analysis of the shear flow problem, J. Rheol., 43(3) (1999), 829-843.
[7] M. G. Forest, Q. Wang and R. Zhou, The flow-phase diagram of Doi-Hess theory for sheared nematic polymers II: Finite shear rates, Rheol. Acta, 44(1) (2004), 80-93.
[8] H. Goldstein, Classical Mechanics, Addison-Wesley, Reading, MA, 1950, pp. 164-166.
[9] S. Z. Hess, Fokker-Planck equation approach to flow alignment in liquid crystals, Z. Naturforsch. Teil, 31A (1976), 1034-1037.
[10] R. G. Larson and H. C. Ottinger, Effect of molecular elasticity on out-of-plane orientations in shearing flows of liquid-crystalline polymers, Macromolecules, 24 (1991), 6270-6282.
[11] R. G. Larson, The Structure and Rheology of Complex Fluids, Oxford University Press, 1999.
[12] R. G. Larson, Arrested tumbling in shearing flows of liquid crystal polymers, Macromolecules, 23 (1990), 3983-3992.
[13] R. Li, T. Tang and P. Zhang, Moving mesh methods in multiple dimensions based on harmonic maps, J. Comput. Phys., 170 (2001), 562-588.
[14] R. Li, T. Tang and P. Zhang, A moving mesh finite element algorithm for singular problems in two and three space dimensions, J. Comput. Phys., 177 (2002), 365-393.
[15] R. Li, C. Luo and P.-W. Zhang, Numerical simulation of Doi model of polymeric fluids, in: Y. Lu, W. Sun and T. Tang (Eds), Advances in Scientific Computing and Applications, Science Press, Beijing, 2004, pp. 258-273.
[16] H. Liu, H. Zhang and P. Zhang, Axial symmetry and classification of stationary solutions of Doi-Onsager equation on the sphere with Maier-Saupe potential, Commun. Math. Sci, 3(2) (2005), 201-218.
[17] H. Z. Tang and T. Tang, Adaptive mesh methods for one- and two-dimensional hyperbolic conservation laws, SIAM J. Numer. Anal., 41 (2003), 487-515.